


## RESEARCH ARTICLE OPEN ACCESS

# Loss Analysis of Halide-Perovskite Solar Cells Deposited on Textured Substrates

Yueming Wang<sup>1</sup>  | Jürgen Hüpkens<sup>1</sup> | Sandheep Ravishankar<sup>1</sup>  | Benjamin Klingebiel<sup>1</sup> | Thomas Kirchartz<sup>1,2</sup> 

<sup>1</sup>IMD3-Photovoltaik, Forschungszentrum Jülich, Jülich, Germany | <sup>2</sup>Faculty of Engineering and CENIDE, University of Duisburg-Essen, Duisburg, Germany

**Correspondence:** Thomas Kirchartz ([t.kirchartz@fz-juelich.de](mailto:t.kirchartz@fz-juelich.de))

**Received:** 19 November 2024 | **Revised:** 18 February 2025 | **Accepted:** 24 February 2025

**Funding:** Helmholtz Association via the Zeitenwende and SolarTap projects and project-oriented funding (POF IV); German Research Foundation (DFG), Grant/Award Number: SPP 2196 491111487-openaccess; HITEC Graduate School (HITEC), Grant/Award Number: Fellowship

**Keywords:** efficiency losses | light management | perovskite | textured substrates | transient photoluminescence

## ABSTRACT

To create efficient perovskite–silicon tandem cells with small pyramidal structures, it is crucial to deposit high-quality wide-bandgap perovskite films on textured surfaces. To attain this objective, it is essential to comprehensively understand the characteristics of perovskite films on textured surfaces and their impact on the efficiency loss mechanisms of perovskite solar cells. We find that the textured substrates provide better absorptance of the perovskite films, thus reducing the efficiency losses resulting from the reflected or transmitted light. The short-circuit current of textured devices reaches 95% of the Shockley–Queisser limit at 1.68 eV. In addition, the fill factor losses are not obviously influenced by the textured bottom surface of the perovskite films. Furthermore, transient photoluminescence was used to quantify the recombination losses at open circuit in layer stacks and full devices, offering insights into the surface recombination velocity at the perovskite/electron transport layer interface and capacitive discharge of the electrodes.

## 1 | Introduction

Lead-halide perovskite semiconductors have attracted significant research interest for photovoltaics over the past decade owing to their properties, such as a sharp optical absorption edge [1] and long diffusion length [2]. Perovskites are promising candidates for combining Si [3], Cu (In, Ga)Se (CIGS) [4], and organic photovoltaics [5] for tandem applications, owing to their advantages of bandgap tunability [6], solution-processed fabrication and low cost [7]. In recent years, monolithic perovskite/Si tandem cells have become a realistic way to overcome the theoretical limitations of single-junction solar cells [8]. These two-terminal (2T) architecture tandem cells suffer from lower parasitic absorption losses compared to three- or four-terminal architecture devices [9, 10]. However, 2T tandem solar cells require good light management to avoid a current mismatch between each subcell [11]. During the rapid development of tandem cells, 2T perovskite/silicon tandem solar cells based on front-side

polished silicon wafers have achieved high efficiencies [12, 13]. However, the random pyramids widely applied in silicon cells for light trapping still need to be maintained in monolithic tandem cells [14]. Recently, the efficiencies of 2T perovskite/silicon tandem solar cells based on textured silicon wafers have surpassed those of polished silicon wafers owing to their enhanced optoelectronic coupling [8, 15]. A fully vacuum [16] or hybrid two-step process [14] allows for the deposition of conformal perovskite films on commercial silicon solar cells, which usually have pyramids larger than 2  $\mu\text{m}$ . However, additives that are important in defect passivation [17], stabilizing wide-bandgap perovskites [18] and controlling crystallization are easily incorporated into solution-based methods but are difficult to include in evaporation techniques. The solution-processed method is therefore still difficult to replace in the fabrication of high-quality perovskite films. Reducing the silicon pyramid size to approximately 1  $\mu\text{m}$  is a viable strategy for growing perovskite films via a solution-processed method that can fully cover small pyramids and

This is an open access article under the terms of the [Creative Commons Attribution](https://creativecommons.org/licenses/by/4.0/) License, which permits use, distribution and reproduction in any medium, provided the original work is properly cited.

© 2025 The Author(s). *Solar RRL* published by Wiley-VCH GmbH.

maintain efficient light management [3, 19]. Moreover, textured silicon bottom cells are less expensive than the excess steps for polishing silicon wafers in industrial applications.

However, it remains a challenge to use solution-processed approaches to deposit high-quality perovskite films on rough surfaces. Hole-transport materials, usually made of molecular semiconductors and employed in p-i-n-type perovskite solar cells, are not easily deposited homogeneously on rough surfaces using solution-processed methods [20]. In addition, the inhomogeneity of the hole-transport layers (HTLs) causes inefficient charge-carrier extraction [21, 22–23]. Self-assembled monolayers (SAMs) are promising materials for solving this problem, especially the SAMs with phosphonic acid molecules in their structures. The phosphonic acid molecules are able to coordinate or covalently bond with transparent conductive oxides (TCOs), which enables sufficient coverage on the textured surface in comparison with organic or polymer HTLs in p-i-n-type perovskite solar cells [4, 24]. The deposition of dense, fully covered perovskite films on textured substrates is another issue that needs to be overcome. Optimizing the DMSO/Pb ratio in the perovskite precursor has been proven to be an efficient strategy [25]. Some research has already reported the fabrication of single-junction perovskite cells on rough surfaces, which are highly relevant to tandem applications with perovskite materials. Farag et al. developed planar perovskite solar cells with close to micrometer-thick perovskite absorber layers that maintain over 18% efficiency using a Lewis base additive [26]. The textured silicon substrate improves light management by reducing the broadband reflectance, which improves the photocurrent of the solar cells. A subsequent study by Farag et al. [27] studied  $V_{oc}$  losses using photoluminescence quantum yield (PLQY) measurements of perovskite solar cells on textured silicon substrates. The authors concluded that the perovskite precursor was important for fabricating high-quality perovskite films on textured substrates. While the research discussed above focuses on either the improved current or  $V_{oc}$  of single-junction perovskite solar cells on textured surfaces, a comprehensive analysis of the efficiency losses of perovskite solar cells on pyramidal-textured surfaces is still lacking.

In this work, we report the fabrication of highly efficient micrometer-thick perovskite solar cells on textured surfaces with a pyramid size of 200–400 nm. The 1.68 eV bandgap opaque perovskite solar cells on textured substrates show a  $J_{sc}$  which is on average 1.5 mA/cm<sup>2</sup> higher than for cells fabricated on planar substrates. Textured substrates improve the absorptance of perovskite films on such surfaces by decreasing reflection, increasing light scattering and thereby improving light absorptance [28, 29–30]. In this study, we investigated the absorptance of perovskite films using PL spectroscopy [31]. We also used a simple method to analyze the losses of the individual photovoltaic parameters of our solar cells based on the Shockley–Queisser (S-Q) model [32, 33], establishing that the efficiency losses are largely attributed to the  $J_{sc}$  losses. Our results highlight the importance of light management in reducing efficiency losses in solar cells. Furthermore, we used transient PL to quantify the recombination losses at open circuit in the layer stacks and full devices. The transient PL provides a way to estimate the surface recombination velocity. The lack of saturation of the differential decay time at low quasi-Fermi-level splitting is

attributed to shallow defects and capacitive discharge of the electrodes in the case of full devices.

## 2 | Results and Discussion

Within the field of perovskite photovoltaics, deposition on rough surfaces is typically associated with the use of perovskite on top of textured silicon wafers in tandem solar cells. However, as the characterization of tandem solar cells provides specific challenges associated with the inability to disentangle effects arising only from one subcell, we designed a test environment in which we could study the optical and electronic effects of rough substrates on perovskite cells with bandgaps that are relevant for tandem solar cells. To achieve this purpose, we fabricated textured substrates by depositing aluminum-doped zinc oxide (AZO) on glass and then etching the AZO to form small textured structures. Subsequently, ITO was sputtered onto the glass/AZO substrates. The perovskite films were deposited via a one-step spin-coating method using an antisolvent. An organic halide salt, 4-fluorophenethyl-ammonium iodide (F-PEAI), was added to the perovskite precursor solution to passivate the defects.

### 2.1 | Absorptance and Steady-State PL Spectra

Good light trapping can improve solar cell performance by reducing the losses due to unabsorbed photons and by reducing the thickness needed for efficient light absorption. Therefore, light trapping can be beneficial for either the short-circuit current density (when comparing equal thicknesses) or open-circuit voltage (if the thicknesses are reduced [34, 35]). Unlike planar substrates, textured substrates allow light to be scattered, thereby passing through the cell at an oblique angle, which increases the likelihood of total internal reflection inside the perovskite film, thereby enabling longer pathlengths of weakly-absorbed light [26]. In the following, we investigate how the use of textured substrates affects light trapping within our perovskite solar cells.

For this purpose, we fabricated micrometer-thick perovskite films on both planar and textured ITO substrates. Figure 1a,b illustrates the two structures of solar cells discussed below. Cross-sectional scanning electron microscopy (SEM) images of the glass/(AZO)ITO/HTL/perovskite stack are shown in Figure S1. The size of the AZO/ITO textures was approximately 200–400 nm vertically so the 1  $\mu$ m perovskite film was thick enough to fully fill the craters.

Short-circuit current density losses in single-junction and tandem solar cells typically result in large efficiency losses [15]. In monolithic perovskite/silicon tandem cells, antireflection layers [36] and textured silicon surfaces [21] are necessary to maximize light coupling in the respective subcells. The absorptance of a perovskite solar cell is intuitively shown in its PL spectrum [37]. The limiting radiative efficiency of a solar cell is calculated using the principle of detailed balance between the absorption and emission of a solar cell in the S-Q theory [38, 39]. The calculations of absorbed and emitted photon fluxes were

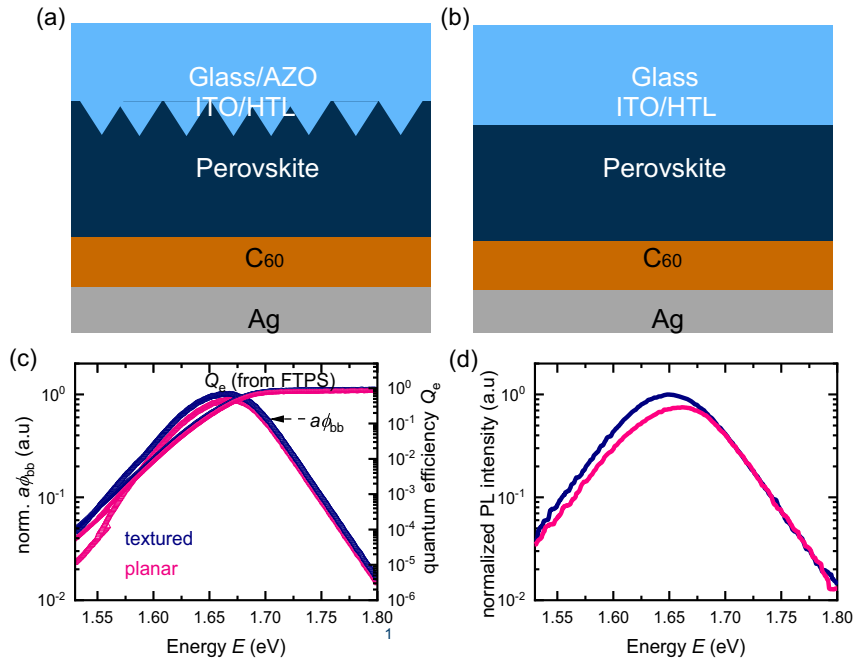


**FIGURE 1** | Schematic of device stack on (a) textured and (b) planar substrates. (c) Normalized signal of FTPS as a function of energy  $E$  for perovskite solar cells based on planar and textured substrates, and external quantum efficiency from FTPS multiplied by the blackbody spectrum. (d) Normalized steady-state PL signal of samples with a glass/AZO/ITO/HTL/perovskite structure, for both planar and textured substrates.

performed while considering the solar cell as a black box with a step function, such as absorptance and emissivity.

The product  $a(E)\phi_{bb}(E)$  is proportional to the luminescence spectrum of the sample, according to the theory of Würfel, which predicts that the PL spectrum  $Y_{PL}(E)$  of a semiconductor approximately follows the relation [40]

$$Y_{PL}(E) = a(E)\phi_{bb}(E) \exp[\Delta E_F/(kT)] \quad (1)$$

where  $\Delta E_F$  is the quasi-Fermi-level splitting,  $kT$  is the thermal energy, and  $a(E)$  is the absorptance of the semiconductor. The primary assumption going into Equation (1) is that the Fermi-level splitting is not a (strong) function of depth within the sample and can therefore be approximated as a single scalar quantity. The blackbody spectrum  $\phi_{bb}(E)$  in units of photons per area [41], time, and energy interval for a planar body emitting into the hemisphere above the body is given by [40]

$$\phi_{bb}(E) = \frac{2\pi E^2}{h^3 c^2} \frac{1}{\exp\left(\frac{E}{kT}\right) - 1} \approx \frac{2\pi E^2}{h^3 c^2} \exp\left(\frac{-E}{kT}\right) \quad (2)$$

Here,  $h$  is the Planck's constant,  $E$  is the photon energy, and  $c$  is the speed of light in vacuum. Equation (1) is a slightly simplified version of Würfel's generalized Planck's law that extends Kirchhoff's law for thermal radiation to non-thermal emission in semiconductors [40, 41–42]. This generalization assumes that the emission originates from the recombination of free electrons and holes, whose occupation can be described by Fermi–Dirac statistics [40, 43, 44].

We characterized the absorptance of opaque cells on planar and textured substrates by Fourier-transform photocurrent spectroscopy (FTPS), which is a highly sensitive method to measure

photocurrent [45]. A comparison of the FTPS spectra in Figure 1c shows that the cell on the textured substrate has a slightly higher absorption than that on the planar substrate, confirming that the small craters can minimize optical losses in our solar cells. Figure 1c shows the product of the absorptance and the blackbody spectrum. In Figure 1d, the steady-state PL spectrum of the sample with structure glass/ITO (AZO)/HTL/perovskite shows a similar behavior as the  $a(E)\phi_{bb}(E)$  in Figure 1c. The PL spectrum of the perovskite on a textured substrate has a higher intensity and shifts to a lower energy compared to that of the perovskite on a planar substrate. This phenomenon is attributed to the enhanced light-trapping capabilities of the textured substrate.

## 2.2 | Solar Cell Performance

We used the triple-cation perovskite  $\text{Cs}_{0.05}\text{FA}_{0.8}\text{MA}_{0.15}\text{PbI}_{2.25}\text{Br}_{0.75}$ , which has a bandgap of 1.68 eV. The opaque devices adopted an ITO/MeO-2PACz:Me-4PACz/PTAA/perovskite/C<sub>60</sub>/BCP/Ag structure. The statistical deviations of the photovoltaic parameters for perovskite solar cells on planar and textured substrates are summarized in Figure 2a–d. The average open-circuit voltage  $V_{oc}$  of the textured samples was 1.166 V, which is lower than that of the planar samples (1.178 V). The fill factor ( $FF$ ) values of the cells on the two different types of substrates were almost in the same value range of approximately 80%. Compared to the cells on planar substrates, the average short-circuit current  $J_{sc}$  of cells on textured substrates was approximately 2 mA/cm<sup>2</sup> higher. The increase in  $J_{sc}$  boosted the average efficiency of the cells on textured substrates, which was 1.5% higher than that on planar substrates, as shown in Figure 2d. The external quantum efficiency (EQE) spectrum in Figure 2f reveals a better absorption of the textured cells in the long wavelength regions, which contributes to the increase in  $J_{sc}$  shown in the  $J$ – $V$  curves

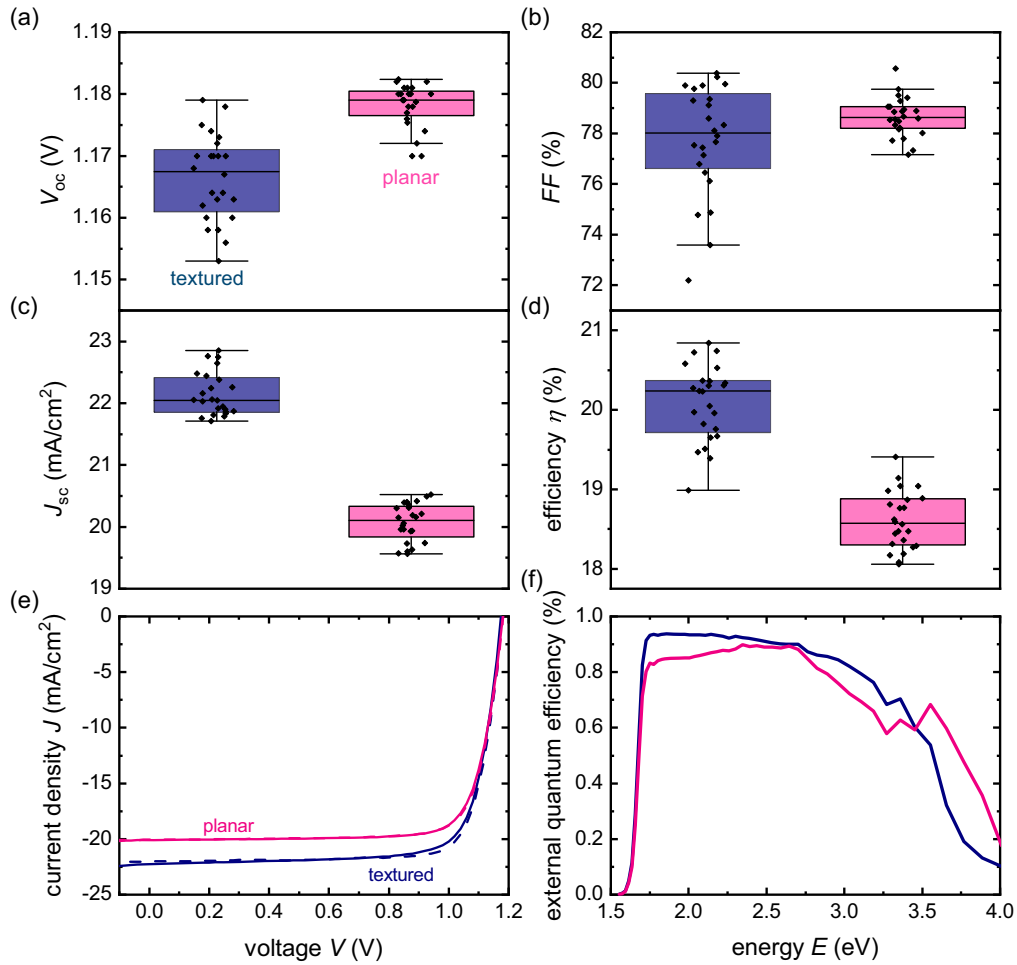


**FIGURE 2** | The statistics of (a) open-circuit voltage  $V_{oc}$ , (b)  $FF$ , (c) short-circuit current  $J_{sc}$ , and (d) efficiency for the cells on planar and textured substrates. (e) Illuminated current–voltage curve of a 1  $\mu\text{m}$  thick perovskite solar cell on planar and textured substrates measured with an AAB sun simulator in forward (solid lines) and backward scan (dash lines) directions. (f) EQE spectra for perovskite solar cells with the same structure as shown in Figure 2e.

(Figure 2e). In addition, we tracked a short-time maximum power point of the devices under 1 sun illumination with a white LED light source at room temperature in  $\text{N}_2$  atmosphere (Figure S7). Compared to the planar device, the textured device exhibited better operational stability.

### 2.3 | Efficiency Loss Analysis

We studied the loss mechanism in solar cells on planar and textured substrates by comparing the photovoltaic parameters  $J_{sc}$ ,  $V_{oc}$ ,  $FF$ , and efficiency of a cell with the expected values of an idealized cell with the same bandgap using the S–Q model [32, 33]. In Figure 3a,b, we compare the power density curves of the illuminated  $J$ – $V$  characteristics (black line), the associated cells with ideal  $FF$  (red lines), and the 1.68 eV cell in the S–Q model (blue lines). Figure 3c shows the ratio of the different losses for the devices on planar and textured substrates. The normalized efficiency is written as [32, 33]

$$\frac{\eta_{\text{real}}}{\eta_{\text{SQ}}} = \frac{J_{sc}}{J_{sc}^{\text{SQ}}} \frac{V_{oc}^{\text{real}}}{V_{oc}^{\text{SQ}}} \frac{FF_0(V_{oc}^{\text{real}})}{FF_0(V_{oc}^{\text{SQ}})} \frac{FF_{\text{real}}}{FF_0(V_{oc}^{\text{real}})} \quad (3)$$

The yellow part in Figure 3c shows the loss due to imperfect photocurrent  $J_{sc}/J_{sc}^{\text{SQ}}$ . The SQ efficiency of the device on the planar substrate is only 87% owing to the high photocurrent loss, while the device on the textured substrate can still maintain 95.55% of the SQ limit at 1.68 eV because of better light management. The  $V_{oc}/V_{oc}^{\text{SQ}}$  loss (green in Figure 3c) is the highest loss in cells on both the planar substrate and textured substrate. The  $V_{oc}^{\text{SQ}}$  for the 1.68 eV perovskite solar cell is 1.399 V. The difference between the ideal and real open-circuit voltage  $\Delta V_{oc} = V_{oc}^{\text{SQ}} - V_{oc}$  is 216 mV for the device on the planar substrate and 220 mV for the device on the textured substrate. Thus, there is very little difference in  $V_{oc}$  loss between the two types of samples.

Within the simple logic of an equivalent circuit model of a solar cell, the  $FF$  depends on the ideality factor  $n_{id}$ , series and parallel resistances, and the  $V_{oc}$  of the solar cell. In the limit of an infinitely large parallel resistance, the  $FF$  approximately follows the relation based on the one-diode model of solar cells with perfect ohmic series resistance [46]

$$FF = \frac{v_{oc} - \ln(v_{oc} + 0.72)}{v_{oc} + 1} \left( 1 - R_s \frac{J_{sc}}{V_{oc}} \right) \quad (4)$$

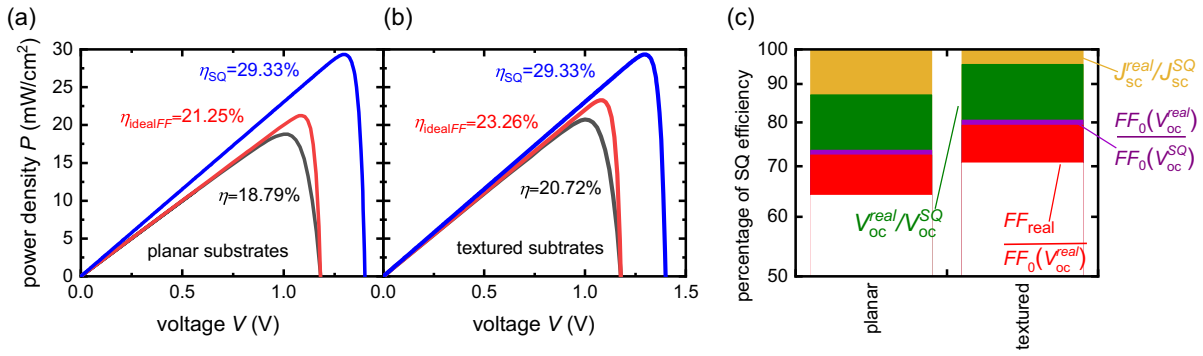


**FIGURE 3** | Power density curves of the illuminated (black lines), ideal  $FF$  at measured  $V_{oc}$  (red lines), and complete SQ model (blue lines) of solar cells on (a) planar substrate and (b) textured substrate. (c) The percentage of S-Q efficiency for cells with different substrates separated in current loss ( $J_{sc}/J_{sc}^{SQ}$ ), voltage loss ( $V_{oc}^{real}/V_{oc}^{SQ}$ ), and  $FF$  losses ( $FF_{real}/FF_0(V_{oc}^{real})$ ,  $FF_0(V_{oc}^{real})/FF_0(V_{oc}^{SQ})$ ) on a logarithmic scale.

The normalized open-circuit voltage is defined as  $v_{oc} = qV_{oc}/(n_{id}kT)$ , with  $k$  being the Boltzmann constant,  $q$  the elementary charge,  $T$  the temperature of the solar cell, and  $R_s$  the series resistance. The loss in  $FF$  will be discussed in two parts: one part is the  $FF$  loss due to  $\Delta V_{oc}$ , given by  $FF_0(V_{oc}^{real})/FF_0(V_{oc}^{SQ})$  under the premise of  $R_s = 0$  and  $n_{id} = 1$  (purple in Figure 3c) and the other part is the  $FF$  loss from  $n_{id}$  and  $R_s$ , given by  $FF_{real}/FF_0(V_{oc}^{real})$  (red in Figure 3c).

The yellow, green, and purple columns in Figure 3c summarize the loss between the blue and red curves in Figure 3a,b. The planar device has 72.46% of  $\eta_{SQ}$  while the textured device has 79.3% of  $\eta_{SQ}$  up to now. The influence of the resistance and ideality factors on the cell performance was investigated separately.

The series resistance effects in real solar cells usually originate from the lateral current transport in the metal oxide and metal electrodes, as well as the limited conductivity of intrinsic perovskite absorbers and charge-transport layers. The series resistance increases with increasing current flow through the diode; hence, it is more important at higher currents. The parallel resistance can also reduce the performance of solar cells. However, the parallel resistance in the dark is typically high enough not to matter for the one sun operation of a solar cell [47]. Here, we discuss a method to quantify  $R_s$  and the  $FF$  loss from  $R_s$ .

A convenient approach to determine the voltage-dependent series resistance is to compare the current-voltage curves under illumination and in the dark [48–50]. When involving the series resistance but ignoring the parallel resistance, the current-voltage curve of a solar cell under illumination is written as

$$J_i = J_0 \left( \exp \left( \frac{q(V_i - J_i R_s)}{n_{id} k T} \right) - 1 \right) - J_{sc} \quad (5)$$

where  $J_0$  is the saturation current density of the solar cell. The current-voltage curve in the dark is written in the same logic as before, as

$$J_d = J_0 \left( \exp \left( \frac{q(V_d - J_d R_s)}{n_{id} k T} \right) - 1 \right) \quad (6)$$

The differences between Equations (5) and (6) are the voltage drop over the series resistance and the  $J_{sc}$  missing in the dark

current-voltage equation (Figure S3). For equal current densities, the series resistance is determined from the difference between  $V_i$  and  $V_d$  as follows:

$$R_s = (V_d - V_i)/J_{sc} \quad (7)$$

Figure 4a shows the voltage-dependent  $R_s$  values of solar cells on planar and textured substrates calculated from Equation (7). The values of  $R_s$  were high at lower voltages because of increasing internal resistance. At higher voltages (above 1.15 V),  $R_s$  decreases and moves to a flat region. The average values of  $R_s$  in a voltage range from 1.15 to 1.2 V are 5.01  $\Omega \text{ cm}^2$  for the planar device and 4.2  $\Omega \text{ cm}^2$  for the textured device.  $J_{sc}$  and  $V_{oc}$  measured as a function of light intensity (Suns- $V_{oc}$ ) provide an  $R_s$ -free version of the diode equation:

$$J_{sc} = J_0 \left( \exp \left( \frac{qV_{oc}}{n_{id} k T} \right) - 1 \right) \quad (8)$$

The  $FF$  extracted from the Suns- $V_{oc}$  curve (red lines in Figure S4) is the  $FF$  without loss from  $R_s$  ( $FF_{J_{sc}V_{oc}}$ ). The difference in  $FF_{J_{sc}V_{oc}}$  and  $FF$  from the illuminated  $J$ - $V$  curve reveals the loss due to series resistance in the cell  $\Delta FF_{R_s} = FF_{J_{sc}V_{oc}} - FF$  ( $\Delta FF_{R_s}$  are listed in Table S1).

The Suns- $V_{oc}$  curve is useful for determining  $n_{id}$ , which was calculated by fitting of  $\ln(J_{sc})$  and  $V_{oc}$ .

$$n_{id} = qdV_{oc}/[kT \ln J_{sc}] \quad (9)$$

Figure 4b shows the voltage-dependent  $n_{id}$  of the cells on different substrates. The average values of  $n_{id}$  were calculated between 1.15 V to 1.16 V for the device on the planar substrate and 1.17 V for the textured device. The  $n_{id}$  values of the two samples are almost the same and are much lower than 2, which suggests that the recombination mechanism is mainly from shallow defects [51]. The  $FF$  losses  $\Delta FF_{n_{id}} = FF_{id} - FF_{J_{sc}V_{oc}}$  originating from the ideality factor being  $>1$  are listed in Table S1. The parameter  $FF_{id}$  represents the  $FF$  values that could be obtained in the absence of series-resistance losses and non-unity ideality factors.

To quantify and analyze efficiency losses due to the series resistance and ideality factor, we compared the power densities of the



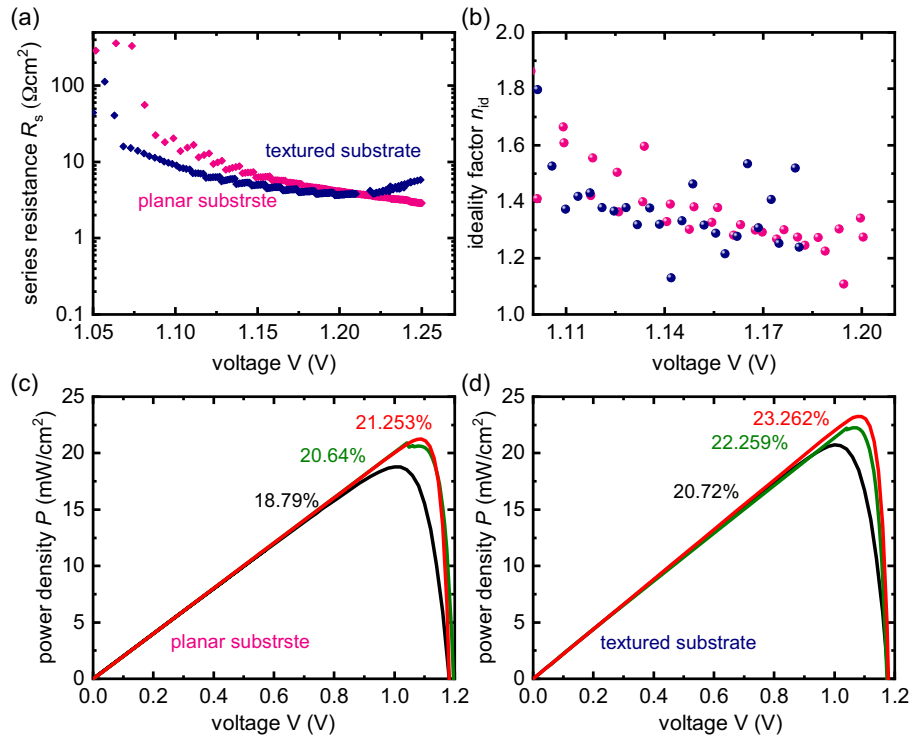


**FIGURE 4** | (a) Series resistance calculated from the difference between the dark and illuminated  $J$ - $V$  curve. (b) Ideality factor  $n_{id}$  derived from the Suns- $V_{oc}$  measurement. Power density curves of the illuminated (black lines),  $J_{sc}V_{oc}$  (green lines), and ideal FF (red lines) perovskite solar cells on a (c) planar substrate and (d) textured substrate.

illuminated  $J$ - $V$  curves (black), the reconstructed power densities of  $J_{sc}V_{oc}$  curves at different light intensities (green) and the power density curves of cells with ideal FF at measured  $J_{sc}$  and  $V_{oc}$  (red), as shown in Figure 4c,d. The efficiency losses from  $R_s$  are 1.85% and 1.54% for the planar and textured cells, respectively. The losses due to the non-ideal diode behavior were 0.613% for the planar device and 1% for the textured device. The different values of the red and black curves in Figure 4c,d correspond to the red part in Figure 3c.

## 2.4 | Transient PL

Transient PL has frequently been used to analyze the charge-carrier dynamics of perovskite films and can also be used to study layer stacks and full devices; however, the latter requires more complicated data interpretation approaches [37, 52]. Transient PL was measured using a gated charge-coupled-device (CCD) camera-based detection setup on full devices with the layer stack glass (AZO)/ITO/HTL/perovskite/ $C_{60}$ /BCP/Ag and on layer stacks of the type glass (AZO)/ITO/HTL/perovskite to study the effect of textured and planar substrates on the recombination dynamics within halide perovskites. The detection method using the gated CCD was chosen to enable a relatively high dynamic range of data that is significantly higher than that of most datasets obtained with time-correlated single photon-counting setups [37, 51, 52].

The normalized time-resolved photoluminescence (tr-PL) decays measured on the planar and textured samples are plotted on a log-log scale in Figure 5a. The planar sample exhibited a slightly

faster decay than the textured sample at longer measurement times, regardless of the presence of full cells or half cells. To calculate the differential decay time  $\tau_{diff}$ , the following equation is used.

$$\tau_{diff} = -2 \left( \frac{d \ln(\phi)}{dt} \right)^{-1} \quad (10)$$

where  $\phi$  is the intensity of luminescence and the factor 2 represents the expectation that lead-halide perovskites are typically undoped, i.e.,  $\phi \propto np = n^2$ . Here,  $n$  is the charge-carrier concentration for the equal electron ( $n$ ) and hole ( $p$ ) densities during the PL transients. The differential decay time  $\tau_{diff}$  as a function of quasi-Fermi-level splitting  $\Delta E_F$  is plotted in Figure 5b.  $\Delta E_F$  is proportional to  $\ln(\phi)$ . Higher values of  $\Delta E_F$  correspond to earlier times after the laser pulse, when radiative and Auger recombination or charge extraction through the charge transport layer toward the electrode affect the differential decay time. The differential decay times of half cells (solid circles) continuously increase and do not saturate at lower  $\Delta E_F$ , as one would expect to happen in a situation where deep defects dominate recombination [52]. Thus, the continuous change in decay time indicates that a recombination process that is superlinear in charge-carrier density dominates the decay. As discussed in ref. [51], the most likely explanation for such data is that there are shallow defects that not only trap charge carriers from one band but dominate recombination (i.e., trap charge carriers from both bands) [51]. Shallow defects start to be charged only under sufficient illumination (photodoping) or forward bias [53]. At longer times (lower  $\Delta E_F$ ), these charged defects re-emit their charge carriers to the band. Thus, the decay time continuously increases for low carrier densities or low quasi-Fermi-level splitting.

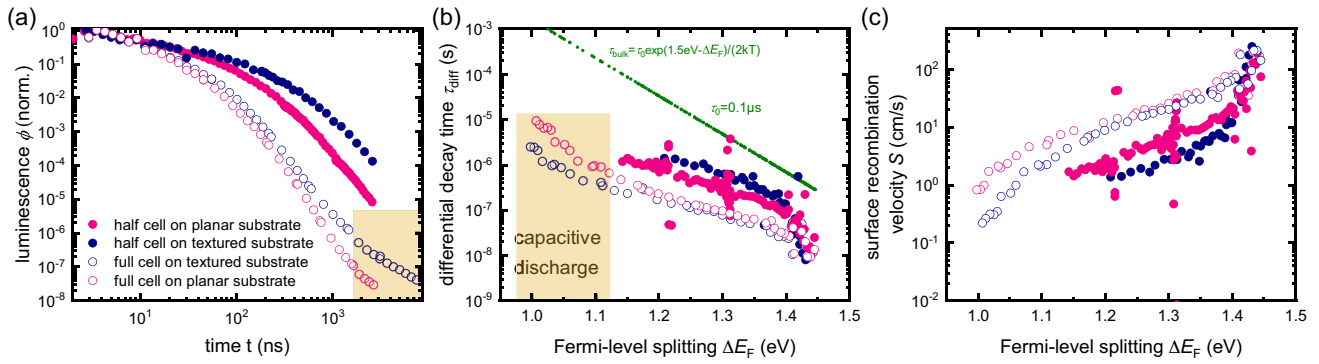


**FIGURE 5** | (a) Normalized transient PL of full-cell glass/ITO/Me-4PACz:MeO-2PACz/PTAA/perovskite/C<sub>60</sub>/BCP/Ag and half-cell glass/ITO/Me-4PACz:MeO-2PACz/PTAA/perovskite measured with a gated CCD detection setup. (b) Differential decay time calculated from normalized transient PL and plotted against Fermi-level splitting. (c) Estimated surface recombination velocity  $S_{rec,int}$  using Equation (11), assuming  $\tau_0 = 0.1 \mu s$ .

The two samples show similar  $\tau_{diff}$  from high  $\Delta E_F$  to  $\Delta E_F$  approximately equal to  $V_{oc}$ . The  $\tau_{diff}$  of the textured half cell is higher than the planar one at the range of  $\Delta E_F$  lower than  $V_{oc}$ .

For the corresponding full cells, the values of  $\tau_{diff}$  (open circles) are one order of magnitude lower than those of the half cells (solid circles) which is related to an increase in interface recombination at the perovskite/C<sub>60</sub> interface. This is a phenomenon frequently seen in the literature [54, 55–56]. To quantify interface recombination, we aim to extract the surface recombination velocity ( $S_{rec,int}$ ) by considering the carrier density-dependent decay time of the layer stack without the perovskite/C<sub>60</sub> interface. Thus, we use a similar approach as is common in the literature, [57, 58] but evaluate it as a function of Fermi-level splitting or charge-carrier density. The surface recombination velocity is estimated from the voltage-dependent differential decay time via [59]

$$S_{rec,int}(\Delta E_F) = 2d \left( \frac{1}{\tau_{diff}(\Delta E_F)} - \frac{1}{\tau_{bulk}(\Delta E_F)} \right) \quad (11)$$

The bulk recombination lifetime  $\tau_{bulk}$  depends on the Fermi-level splitting. Given that our experimental data show slopes similar to those predicted by the analytical model for shallow defects [51], it is reasonable to express the bulk lifetime via  $\tau_{bulk} = \tau_0 \exp(1.5eV - \Delta E_F)/(2kT)$ , with  $\tau_0$  being a prefactor that shifts the bulk lifetime up and down but does not alter the slope, 1.5 eV is chosen as a value of maximum  $\Delta E_F$ . The plot of  $\tau_{bulk}$  versus  $\Delta E_F$  using a value of  $\tau_0 = 0.1 \mu s$  is shown in Figure 5b. Here,  $\tau_0 = 0.1 \mu s$  is chosen for  $\tau_{bulk}$  to be strictly above the data, as otherwise the assumed  $\tau_{bulk}$  would be inconsistent with observations. However, from the data, we cannot know how much above the observed decay times the bulk lifetime should be. We now use this relatively arbitrary value of  $\tau_0 = 0.1 \mu s$  to estimate the surface recombination velocity using Equation (11). We note that the result is therefore affected by the measured data and an assumption, so we must assign a lower degree of confidence to  $S_{rec,int}$  than we would do to directly measure the decay time.

The estimated surface recombination velocity  $S_{rec,int}$  versus  $\Delta E_F$  is shown in Figure 5c. The values of  $S_{rec,int}$  that result from assuming different values for  $\tau_0$  are shown in Figure S5 and S6. In half cells, the planar sample has values of  $S_{rec,int}$  that

are higher than for the textured sample for almost the entire range of quasi-Fermi-level splitting. For the full cells, the planar and textured cells have a similar value of  $S_{rec,int}$ . The remaining slope of  $S_{rec,int}$  ( $\Delta E_F$ ) could originate from the interfacial traps being shallow with respect to either of the bands. Alternatively, the slope could also originate from our assumption that the bulk lifetime follows a simple shape  $\sim \exp(-\Delta E_F/(2kT))$ .

In addition, the full cells show a longer decay time than the half-cells at very low Fermi-level splitting. The  $\tau_{diff}$  of the full cells continuously increases for values of  $\Delta E_F < 1.1$  eV as shown in Figure 5b (marked light yellow area in Figure 5a,b). This phenomenon is caused by the discharging of the electrode capacitance in the full cells. At low carrier densities (and long times during the transient), the electrons and holes that flow to the electrodes at early times are re-injected from the electrodes and flow toward the absorber. Within the absorber and at its interfaces to the transport layers, these reinjected charge carriers will eventually recombine. As the recombination resistance of any diode increases toward lower forward biases (the diode becomes more resistive), the  $RC$  time constant of the electrode discharging via the diode continually increases. It can notably increase to values that are significantly higher than the actual recombination lifetime [60].

The carrier recombination dynamics during a transient can be described by a differential equation in time [61]

$$\frac{dn(t)}{dt} = \frac{G - k_{rad}n(t)^2 - n(t)/\tau_{SRH}}{1 + n_Q/n(t)} \quad (12)$$

with  $n_Q = 2C_{area}kT/(q^2d)$  being the charge per volume that is included on the capacitor,  $C_{area}$  is the area-related capacitance in unit of F/cm<sup>2</sup>,  $G$  is the generation rate,  $k_{rad}$  is the radiative recombination coefficient and  $\tau_{SRH}$  is the Shockly–Read–Hall (SRH) lifetime. Equation (12) includes three effects: radiative recombination, SRH recombination, and the discharge of the contact capacitance that is included via the  $n_Q/n(t)$  term in the denominator of the right-hand side of Equation (12).

In a situation where there are fewer charge carriers in the absorber layer than in the contact layer  $n < n_Q$ , charge-carrier recombination will be delayed because of the need to discharge

the capacitance before carrier recombination can happen. The differential decay time in full cells is written as [61]

$$\tau_{\text{cell,diff}} = -\frac{n(t)}{dn(t)/dt} = \frac{n_Q/n(t) + 1}{k_{\text{rad}}n(t) + 1/\tau_{\text{SRH}}} \quad (13)$$

When the carrier concentration is low ( $n \ll n_Q$ ), the capacitive effects dominate the recombination processes, which is relevant for times  $t > 10^3$  ns in Figure 5a and  $\Delta E_F < 1.1$  eV in Figure 5b. The differential decay time of full cells is then simplified to  $\tau_{\text{cell,diff}} = n_Q \tau_{\text{SRH}}/n$  from Equation (13). The slight change of slope in the data for the full cells at around 1.1 eV Fermi-level splitting is likely the transition from bulk recombination affected by shallow defects to charge-carrier re-injection from the electrodes followed by recombination via shallow defects. This change of slope is a phenomenon that has been previously observed, for instance, in Figure 4d of ref. [51].

## 2.5 | Numerical Simulations of Transient PL

To establish a better understanding of the effect of shallow traps in the bulk and interface recombination, we performed a range of numerical simulations (using SETFOS developed by Fluxim AG) of the transient PL experiments on complete solar cells. For this purpose, we assumed that we have a uniform distribution of acceptor-like shallow defects in the bulk that causes the continuously changing decay times that we observe in the experiments shown in Figure 5, as well as in all other experiments on films, layer stacks, and full devices that we have performed on lead-halide perovskites with similar compositions [51, 59, 62, 63]. In addition, we add a defect at the perovskite- $\text{C}_{60}$  interface that we assume to either vary in energetic position or in its associated interface recombination velocity. Figure 6a shows the effect of variation of the trap depth for a surface recombination velocity of  $S_{\text{rec,int}} = 1000$  cm/s. We see that the deeper the interfacial trap is, the more the continuous but smooth variation of the differential lifetime as a function of  $\Delta E_F$  is changed to show a more step-like behavior, creating a plateau at high  $\Delta E_F$ .

Considering the perovskite layer thickness  $d = 1 \mu\text{m}$ , this plateau corresponds to the interfacial recombination lifetime  $\tau_{\text{rec,int}} = d/S_{\text{rec,int}} = 10^{-7}$  s. Figure 6b shows the effect of a variation of the surface recombination velocity, assuming a deep defect at the interface. Higher surface recombination velocities create a plateau at high  $\Delta E_F$  due to the dominance of the interface recombination (corresponding  $\tau_{\text{rec,int}}$  values shown as dashed lines), while lower surface recombination velocities maintain the continuous variation of the decay time that is observed for lower  $\Delta E_F$  values. From these simulations, we can conclude that the shape of the decay time spectra at high  $\Delta E_F$  for full cells (Figure 5b) is consistent with the relatively low surface recombination velocities for recombination at the perovskite/ $\text{C}_{60}$  interface that are calculated in Figure 5c.

## 3 | Conclusion

A necessary challenge to overcome to achieve highly efficient silicon-perovskite tandem cells is depositing perovskites with bandgaps slightly lower than 1.7 eV on textured surfaces in such a way that they fully cover the textured bottom cell surface. We fabricated 1.68 eV bandgap opaque perovskite solar cells with micrometer thickness on both planar substrates and textured substrates with pyramid sizes of 200–400 nm. The solar cells on textured substrates show a 2 mA/cm<sup>2</sup> higher average  $J_{\text{sc}}$  compared to those on planar substrates, attributed to better absorbance of the perovskite films on the textured surface. In this study, we quantify the losses of individual photovoltaic parameters using the S-Q model and highlight the importance of light management in reducing efficiency losses. The  $FF$  losses are not obviously influenced by the morphology of the perovskite bottom surface. Transient PL was used to quantify recombination losses at open circuit in layer stacks and full cells, providing information about the surface recombination velocity and long differential decay lifetime, likely caused by shallow defects in the bulk or more likely the interface between the absorber and the two transport layers. The morphology of the substrates does not influence the surface recombination. For the complete cell,

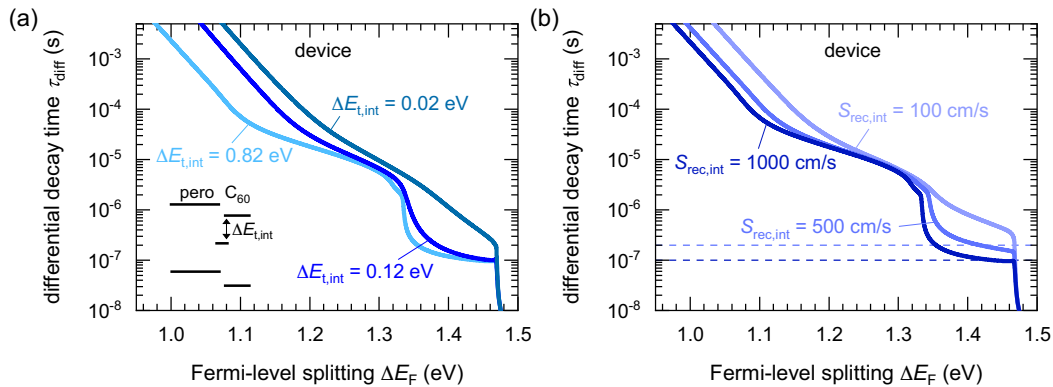


**FIGURE 6** | Calculated differential decay times from drift-diffusion simulations of the transient PL spectra of a ITO/Me-4PACz:MeO-2PACz/PTAA/perovskite/ $\text{C}_{60}$ /BCP/Ag device. (a) The variation of the decay time versus the perovskite/ $\text{C}_{60}$  interface trap energy-level  $E_{\text{t,int}}$ , defined using an energy offset  $\Delta E_{\text{t,int}}$  from the conduction band of the  $\text{C}_{60}$  layer (i.e.  $\Delta E_{\text{t,int}} = E_{\text{c,C}_{60}} - E_{\text{t,int}}$ ). An interface recombination velocity of  $S_{\text{rec,int}} = 1000$  cm/s was used. (b) The variation of the decay time for different values of  $S_{\text{rec,int}}$  for a trap at the perovskite/ $\text{C}_{60}$  interface with  $\Delta E_{\text{t,int}} = 0.82$  eV. The dashed lines indicate the corresponding interface recombination lifetime  $\tau_{\text{rec,int}}$  for a given  $S_{\text{rec,int}}$  ( $\tau_{\text{rec,int}} = d_{\text{pero}}/S_{\text{rec,int}}$ ). In both cases, a uniform distribution of shallow traps in the bulk of the perovskite at a depth of 0.2 eV from the perovskite conduction band was used.



the long lifetimes are partly caused by capacitive discharge of the electrodes, which can be identified from a change in the slope of the decay time versus carrier density or Fermi-level splitting.

## Acknowledgments

The authors acknowledge support from the Helmholtz Association via the Zeitenwende and SolarTap projects and project-oriented funding (POF IV). The authors also acknowledge funding from the German Research Foundation (DFG) for the project CREATIVE within the SPP “Perovskite Semiconductors: From Fundamental Properties to Devices” (SPP 2196). Open access publication was funded by the DFG491111487. Y.W. acknowledges the HITEC graduate school for a HITEC Fellowship.

## Conflicts of Interest

The authors declare no conflicts of interest.

## Data Availability Statement

The data that support the findings of this study are available from the corresponding author upon reasonable request. All simulation files are uploaded to the Zenodo database with the identifier 10.5281/zenodo.14963238.

## References

1. S. De Wolf, J. Holovsky, S.-J. Moon, et al., *The Journal of Physical Chemistry Letters* 5 (2014): 1035.
2. S. D. Stranks, G. E. Eperon, G. Grancini, et al., *Science* 342 (2013): 341.
3. Y. Hou, E. Aydin, M. De Bastiani, et al., *Science* 367 (2020): 1135.
4. A. Al-Ashouri, A. Magomedov, M. Roß, et al., *Energy & Environmental Science* 12 (2019): 3356.
5. X. Wang, D. Zhang, B. Liu, et al., *Advanced Materials* 35 (2023): 2305946.
6. E. L. Unger, L. Kegelmann, K. Suchan, D. Sörell, L. Korte, and S. Albrecht, *Journal of Materials Chemistry A* 5 (2017): 11401.
7. M. Cai, Y. Wu, H. Chen, X. Yang, Y. Qiang, and L. Han, *Advanced Science* 4 (2017): 1600269.
8. E. Aydin, T. G. Allen, M. De Bastiani, et al., *Science* 383 (2024): eadh3849.
9. S. Gharibzadeh, I. M. Hossain, P. Fassel, et al., *Advanced Functional Materials* 30 (2020): 1909919.
10. F. Gota, M. Langenhorst, R. Schmager, J. Lehr, and U. W. Paetzold, *Joule* 4 (2020): 2387.
11. M. Singh, R. Santbergen, I. Syifai, A. Weeber, M. Zeman, and O. Isabella, *Nanophotonics* 10 (2020): 2043.
12. S. Mariotti, E. Köhnen, F. Scheler, et al., *Science* 381 (2023): 63.
13. A. Al-Ashouri, E. Köhnen, B. Li, et al., *Science* 370 (2020): 1300.
14. X. Y. Chin, D. Turck, J. A. Steele, et al., *Science* 381 (2023): 59.
15. E. Aydin, E. Ugur, B. K. Yildirim, et al., *Nature* 623 (2023): 732.
16. L. Gil-Escrig, M. Roß, J. Sutter, A. Al-Ashouri, C. Becker, and S. Albrecht, *Solar RRL* 5 (2021): 2000553.
17. G. Yang, Z. Ni, Z. J. Yu, et al., *Nature Photonics* 16 (2022): 588.
18. J. Xu, C. C. Boyd, Z. J. Yu, et al., *Science* 367 (2020): 1097.
19. P. Tockhorn, J. Sutter, A. Cruz, et al., *Nature Nanotechnology* 17 (2022): 1214.

20. N. Camaioni, C. Carbonera, L. Ciammaruchi, et al., *Advanced Materials* 35 (2023): 2210146.
21. F. Sahli, J. Werner, B. A. Kamino, et al., *Nature Materials* 17 (2018): 820.
22. S. M. Park, M. Wei, N. Lempeis, et al., *Nature* 624 (2023): 289.
23. L. Mao, T. Yang, H. Zhang, et al., *Advanced Materials* 34 (2022): 2206193.
24. M. Li, M. Liu, F. Qi, F. R. Lin, and A. K. Y. Jen, *Chemical Reviews* 124 (2024): 2138–2204.
25. B. Chen, J. Y. Zhengshan, S. Manzoor, et al., *Joule* 4 (2020): 850.
26. A. Farag, R. Schmager, P. Fassel, et al., *ACS Applied Energy Materials* 5 (2022): 6700.
27. A. Farag, P. Fassel, H. Hu, et al., *Advanced Functional Materials* 33 (2023): 2210758.
28. Z. C. Holman, M. Filipič, A. Descoeudres, et al., *Journal of Applied Physics* (2013): 113.
29. H. Li, Y. Hu, H. Wang, Q. Tao, Y. Zhu, and Y. Yang, *Solar RRL* 5 (2021): 2000524.
30. H. Sai, Y. Kanamori, K. Arafune, Y. Ohshita, and M. Yamaguchi, *Progress in Photovoltaics: Research and Applications* 15 (2007): 415.
31. C. Barugkin, T. Allen, T. K. Chong, T. P. White, K. J. Weber, and K. R. Catchpole, *Optics Express* 23 (2015): A391.
32. J.-F. Guillemoles, T. Kirchartz, D. Cahen, and U. Rau, *Nature Photonics* 13 (2019): 501.
33. L. Krückemeier, U. Rau, M. Stölterfoht, and T. Kirchartz, *Advanced Energy Materials* 10 (2020): 1902573.
34. T. Kirchartz, L. Krückemeier, and E. L. Unger, *APL Materials* (2018): 6.
35. U. Rau, U. W. Paetzold, and T. Kirchartz, *Physical Review B* 90 (2014): 035211.
36. J. Zheng, C. F. J. Lau, H. Mehrvarz, et al., *Energy & Environmental Science* 11 (2018): 2432.
37. T. Kirchartz, J. A. Márquez, M. Stölterfoht, and T. Unold, *Advanced Energy Materials* 10 (2020): 1904134.
38. W. Shockley and H. J. Queisser, *Journal of Applied Physics* 32 (1961): 510.
39. W. van Roosbroeck and W. Shockley, *Physical Review* 94 (1954): 1558.
40. P. Würfel, *Journal of Physics C: Solid State Physics* 15 (1982): 3967.
41. M. Planck, *Annalen der Physik* 309 (1901): 553.
42. G. Kirchhoff, *The London, Edinburgh, and Dublin Philosophical Magazine and Journal of Science* 20 (1860): 1.
43. K. Schick, E. Daub, S. Finkbeiner, and P. Würfel, *Applied Physics A* 54 (1992): 109.
44. P. Würfel, S. Finkbeiner, and E. Daub, *Applied Physics A* 60 (1995): 67.
45. T. C. M. Müller and T. Kirchartz, *Absorption and Photocurrent Spectroscopy with High Dynamic Range*, In *Advanced Characterization Techniques for Thin Film Solar Cells* (eds. D. Abou-Ras, T. Kirchartz and U. Rau). (2016): p. 189–214.
46. M. A. Green, *Solar Cells* 7 (1982): 337.
47. D. Grabowski, Z. Liu, G. Schöpe, U. Rau, and T. Kirchartz, *Solar RRL* 6 (2022): 2200507.
48. M. Wolf and H. Rauschenbach, *Advanced Energy Conversion* 3 (1963): 455.
49. T. C. Müller, B. E. Pieters, U. Rau, and T. Kirchartz, *Journal of Applied Physics* 113 (2013): 134503.
50. N. Mundhaas, Z. J. Yu, K. A. Bush, et al., *Solar RRL* 3 (2019): 1800378.

51. Y. Yuan, G. Yan, C. Dreessen, et al., *Nature Materials* 23 (2024): 391.
52. L. Krückemeier, B. Krogmeier, Z. Liu, U. Rau, and T. Kirchartz, *Advanced Energy Materials* 11 (2021): 2003489.
53. S. Feldmann, S. Macpherson, S. P. Senanayak, et al., *Nature Photonics* 14 (2020): 123.
54. M. Stolterfoht, C. M. Wolff, J. A. Márquez, et al., *Nature Energy* 3 (2018): 847.
55. J. Warby, F. Zu, S. Zeiske, et al., *Advanced Energy Materials* 12 (2022): 2103567.
56. C. M. Wolff, P. Caprioglio, M. Stolterfoht, and D. Neher, *Advanced Materials* 31 (2019): 1902762.
57. J. Tong, Q. Jiang, A. J. Ferguson, et al., *Nature Energy* 7 (2022): 642.
58. J. Wang, W. Fu, S. Jariwala, I. Sinha, A. K. Y. Jen, and D. S. Ginger, *ACS Energy Letters* 4 (2019): 222.
59. Y. Wang, S. Akel, B. Klingebiel, and T. Kirchartz, *Advanced Energy Materials* 14 (2024): 2302614.
60. D. Kiermasch, A. Baumann, M. Fischer, V. Dyakonov, and K. Tvingstedt, *Energy & Environmental Science* 11 (2018): 629.
61. L. Krückemeier, Z. Liu, B. Krogmeier, U. Rau, and T. Kirchartz, *Advanced Energy Materials* 11 (2021): 2102290.
62. J. Siekmann, A. Kulkarni, S. Akel, et al., *Advanced Energy Materials* 13 (2023): 2300448.
63. Y. Yuan, G. Yan, C. Dreessen, and T. Kirchartz, *Advanced Energy Materials* 15 (2025): 2403279.

### Supporting Information

Additional supporting information can be found online in the Supporting Information section.